

## Article

# Preparation and Application of Amino-Terminated Hyperbranched Magnetic Composites in High-Turbidity Water Treatment

Yuan Zhao <sup>1</sup>, Qianlong Fan <sup>2,\*</sup>, Yinhua Liu <sup>1</sup>, Shuwen Wang <sup>1</sup>, Xudong Guo <sup>1</sup>, Liujia Guo <sup>1</sup>, Mengcheng Zhu <sup>1</sup> and Xuan Wang <sup>1</sup>

<sup>1</sup> College of Chemistry and Chemical Engineering, Henan University of Science and Technology, Luoyang 471000, China

<sup>2</sup> College of Basic Medicine and Forensic Medicine, Henan University of Science and Technology, Luoyang 471000, China

\* Correspondence: fqlong@haust.edu.cn; Tel.: +86-379-64830345

**Abstract:** In order to separate the colloidal in high-turbidity water, a kind of magnetic composite (Fe<sub>3</sub>O<sub>4</sub>/HBPN) was prepared via the functional assembly of Fe<sub>3</sub>O<sub>4</sub> and an amino-terminal hyperbranched polymer (HBPN). The physical and chemical characteristics of Fe<sub>3</sub>O<sub>4</sub>@HBPN were investigated by different means. The Fourier Transform infrared spectroscopy (FTIR) spectra showed that the characteristic absorption peaks positioned at 1110 cm<sup>-1</sup>, 1468 cm<sup>-1</sup>, 1570 cm<sup>-1</sup> and 1641 cm<sup>-1</sup> were ascribed to C–N, H–N–C, N–H and C=O bonds, respectively. The shape and size of Fe<sub>3</sub>O<sub>4</sub>/HBPN showed a different and uneven distribution; the particles clumped together and were coated with an oil-like film. Energy-dispersive spectroscopy (EDS) displayed that the main elements of Fe<sub>3</sub>O<sub>4</sub>/HBPN were C, N, O, and Fe. The superparamagnetic properties and good magnetic response were revealed by vibrating sample magnetometer (VSM) analysis. The characteristic diffraction peaks of Fe<sub>3</sub>O<sub>4</sub>/HBPN were observed at 2θ = 30.01 (220), 35.70 (311), 43.01 (400), 56.82 (511), and 62.32 (440), which indicated that the intrinsic phase of magnetite remained. The zeta potential measurement indicated that the surface charge of Fe<sub>3</sub>O<sub>4</sub>/HBPN was positive in the pH range 4–10. The mass loss of Fe<sub>3</sub>O<sub>4</sub>/HBPN in thermogravimetric analysis (TGA) proved thermal decomposition. The –C–NH<sub>2</sub> or –C–NH persad of HBPN were linked and loaded with Fe<sub>3</sub>O<sub>4</sub> particles by the N–O bonds. When the Fe<sub>3</sub>O<sub>4</sub>/HBPN dosage was 2.5 mg/L, pH = 4–5, the kaolin concentration of 1.0 g/L and the magnetic field of 3800 G were the preferred reaction conditions. In addition, a removal efficiency of at least 86% was reached for the actual water treatment. Fe<sub>3</sub>O<sub>4</sub>/HBPN was recycled after the first application and reused five times. The recycling efficiency and removal efficiency both showed no significant difference five times (*p* > 0.05), and the values were between 84.8% and 86.9%.

**Keywords:** hyperbranched polymer; Fe<sub>3</sub>O<sub>4</sub>; coating; magnetic separation; water treatment



**Citation:** Zhao, Y.; Fan, Q.; Liu, Y.; Wang, S.; Guo, X.; Guo, L.; Zhu, M.; Wang, X. Preparation and Application of Amino-Terminated Hyperbranched Magnetic Composites in High-Turbidity Water Treatment. *Molecules* **2023**, *28*, 6787. <https://doi.org/10.3390/molecules28196787>

Academic Editor: Emmanuel Koudoumas

Received: 22 August 2023

Revised: 17 September 2023

Accepted: 22 September 2023

Published: 24 September 2023



**Copyright:** © 2023 by the authors. Licensee MDPI, Basel, Switzerland. This article is an open access article distributed under the terms and conditions of the Creative Commons Attribution (CC BY) license (<https://creativecommons.org/licenses/by/4.0/>).

## 1. Introduction

The water environment is of vital importance to the sustainable development of mankind [1]. In light of the rapid industrial development, urbanization and growing utilization of chemical materials, as well as the increased concentration of raw turbidity and suspended sediment in water treatment caused by extreme weather (heavy precipitation and floods), water treatment is facing unprecedented challenges, such as black odor, eutrophication, etc. [2–4]. Therefore, it is of great significance to study the separation of suspended particles in high-turbidity water. Kaolin is a kind of typical mineral, and abundant colloidal particles exist in its suspension. The colloidal particles increase the turbidity in solution and are difficult to settle under gravity alone due to the electrostatic interactions.

The major methodologies currently used for separating suspended particles include filtration, centrifugation, flotation, electrophoresis, flocculation, etc. [5–7]. Flocculation is

often applied as a common method, which can be defined as the process by which a solute particle in a solution forms aggregates named flocs. The flocculation process can occur in the mechanisms acting alone or in combination with charge neutralization, electrostatic patch, bridging and sweeping flocculation [8–10]. Magnetic flocculation is a branch of the flocculation technology that removes the pollutants by reaction with magnetic flocculant. The strategies are based on the replacement of traditional flocculant in water treatment by magnetic flocculant. Due to the addition of the magnetic materials, the flocs characterized by a high magnetic susceptibility are formed and separated with the external magnetic field. Moreover, the settling velocity of magnetic floc is much faster under the influence of magnetic force than that in the situation of gravity [11].

In the process of magnetic flocculation separation, the selection of magnetic flocculant plays a key role in improving the separation effect. Typically, it is obtained by the functional assembly of magnetic materials with conventional flocculants, which combines both characteristics of magnetic separation and flocculation simultaneously [12].  $\text{Fe}_3\text{O}_4$  is a common magnetic material which can be used for the functional assembly of flocculants. But single  $\text{Fe}_3\text{O}_4$  nanoparticles are usually insoluble in water, and the flocculation effect could be affected due to agglomeration and precipitation [13,14]. After functional assembly, the resulting magnetic composites not only improve the surface charge and polymerization properties of  $\text{Fe}_3\text{O}_4$  but also improve the electrophoretic mobility and isoelectric point [15]. Polymers including inorganic polymers, organic polymers, and biopolymers are often used in the assembly of magnetic materials [16–18]. Most of these polymers are linear or chained with one or more  $-\text{N}$  group functional groups (e.g.,  $-\text{NH}_2$ ,  $-\text{CONH}_2$ ,  $-\text{N}^+$ ) in the main or branch chains. These functional groups can be grafted onto the surface of  $\text{Fe}_3\text{O}_4$  by electrostatic force and Van Der Waals force to form active sites and improve magnetic separation efficiency [19]. Among the polymers, hyperbranched polymers (HBP) show great potential for the functional assembly with  $\text{Fe}_3\text{O}_4$  due to the highly branched and unique three-dimensional configuration [20–22].

In the three-dimensional quasi-spherical structure of HBP, a large number of internal cavities and active  $-\text{N}$  groups are filled. In functional assembly with  $\text{Fe}_3\text{O}_4$ , supramolecular assemblers with multiple force forms (Van Der Waals forces, hydrogen bonds) are constructed based on the non-covalent interactions of the three-dimensional super-branching structure [23–25]. When reacted with the target pollutant, the magnetic composites showed excellent removal properties by forming electrostatic interactions and hydrogen bond interactions with the analytes [26–28]. The magnetic composites obtained by an embedded assembly of HBP and  $\text{Fe}_3\text{O}_4$  improve the assembly and regeneration stability [29]. In addition, the risk of the active site being replaced or complex reaction during water treatment is overcome, and the adsorption performance of the material is maintained [30].

In the research, amino-terminated hyperbranched magnetic composites were prepared by an embedded assembly of three-dimensional HBPN and  $\text{Fe}_3\text{O}_4$ . The physical and chemical characteristics were analyzed with the methods of FTIR, scanning electron microscopy (SEM), EDS, VSM, XRD, XPS, zeta potential and TGA. Meanwhile, the separation properties of the magnetic nanocomposite were evaluated by applying to the removal and separation of suspended particles in high turbidity water. Also, the recycling and reusing effects were explored.

## 2. Results and Discussion

### 2.1. Characterization of $\text{Fe}_3\text{O}_4/\text{HBPN}$

#### 2.1.1. FTIR

The FTIR spectra of  $\text{Fe}_3\text{O}_4$  and  $\text{Fe}_3\text{O}_4/\text{HBPN}$  are shown in Figure 1. The absorption peak at  $586\text{ cm}^{-1}$  was attributed to the vibration peak of  $\text{Fe}-\text{O}$  [31–33]. For the sample of  $\text{Fe}_3\text{O}_4/\text{HBPN}$ , the peak at  $1468\text{ cm}^{-1}$  was caused by the bending vibration of the  $\text{H}-\text{N}-\text{C}$  bond connected to the amino group [34,35]. In addition, the characteristic absorption peaks corresponding to the  $\text{C}=\text{O}$  and  $\text{N}-\text{H}$  stretching vibrations were observed at  $1641\text{ cm}^{-1}$  and  $1570\text{ cm}^{-1}$  due to the created amido bond [36]. A small peak at  $1189\text{ cm}^{-1}$  was ascribed to

C–N stretching vibration [37,38]. The typical functional bonds of the amino functional group were detected on the spectra of  $\text{Fe}_3\text{O}_4/\text{HBPN}$  in the corresponding position, which indicated that the amino functional group was coated on the surface of  $\text{Fe}_3\text{O}_4/\text{HBPN}$  successfully.

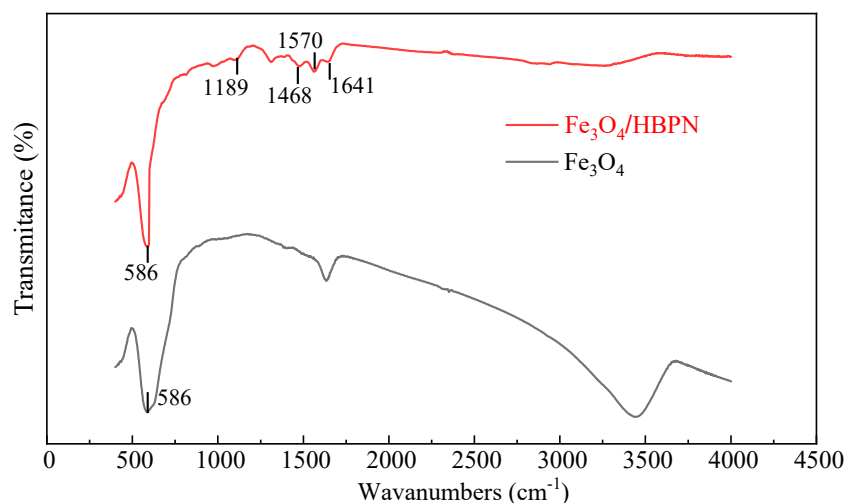


**Figure 1.** FTIR spectra of  $\text{Fe}_3\text{O}_4$  and  $\text{Fe}_3\text{O}_4/\text{HBPN}$ .

### 2.1.2. XRD

In order to analyze the crystalline structure of  $\text{Fe}_3\text{O}_4/\text{HBPN}$  composites, analysis of the XRD spectra of  $\text{Fe}_3\text{O}_4/\text{HBPN}$  was carried out. In the XRD patterns shown in Figure 2,  $\text{Fe}_3\text{O}_4/\text{HBPN}$  showed characteristic diffraction at  $2\theta = 30.01^\circ$ ,  $35.70^\circ$ ,  $43.01^\circ$ ,  $56.82^\circ$ , and  $62.32^\circ$ , corresponding to crystal planes (220), (311), (400), (511), and (440), respectively. The position and relative intensity of the diffraction peaks suitably matched those of the JCPDS card (88-0866) for magnetite [39,40]. This meant that  $\text{Fe}_3\text{O}_4/\text{HBPN}$  still remained an intrinsic phase of magnetite. In addition, the diffraction peaks also matched the JCPDS card (52-1140) for iron silicon oxide [41]. The silicon in  $\text{Fe}_3\text{O}_4/\text{HBPN}$  came from the APTMs, which was one of the most important ingredients for preparation. This result also corroborated the results of EDS.

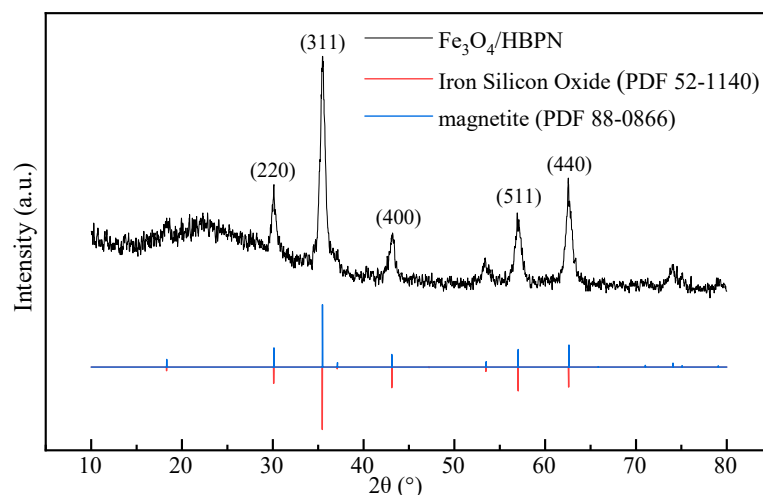


**Figure 2.** X-ray diffraction pattern of  $\text{Fe}_3\text{O}_4/\text{HBPN}$ .

### 2.1.3. XPS

In order to investigate the elemental composition, the chemical oxidation states of surface and near-surface species, the XPS of  $\text{Fe}_3\text{O}_4/\text{HBPN}$  in the survey and high-resolution narrow scan are presented, respectively (Figure 3). From the survey scan in Figure 3a, a

new peak owing to N 1s could be observed on the Fe<sub>3</sub>O<sub>4</sub>/HBPN spectra, which is assigned to the constituent elements of HBPN coated on Fe<sub>3</sub>O<sub>4</sub> surface.

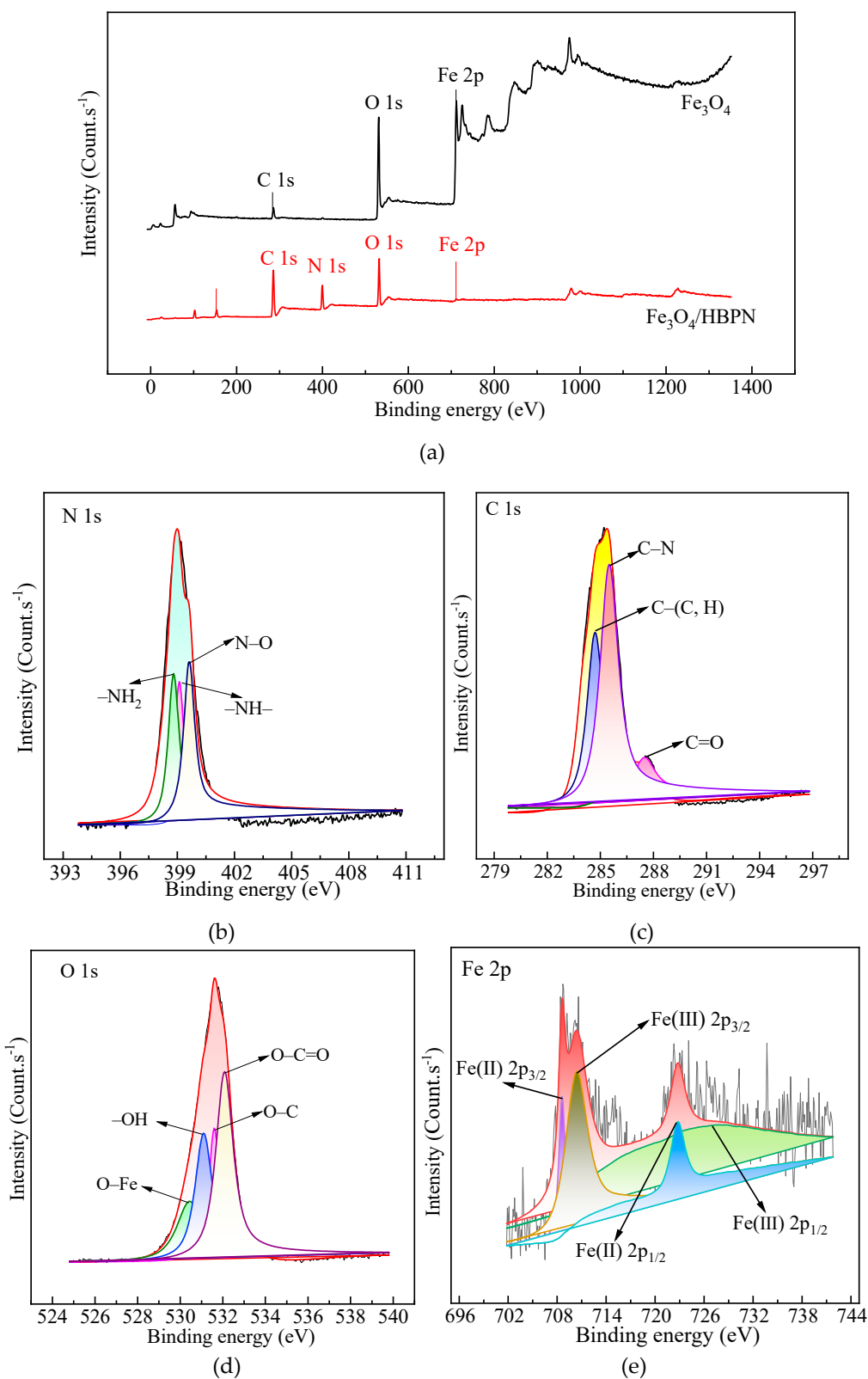


**Figure 3.** X-ray photoelectron spectra (XPS) of Fe<sub>3</sub>O<sub>4</sub> and Fe<sub>3</sub>O<sub>4</sub>/HBPN in the survey scan (a) and high-resolution XPS spectra of Fe 2p (b), C 1s (c), N 1s (d) and O 1s (e) peaks on the surfaces of Fe<sub>3</sub>O<sub>4</sub>/HBPN.

The N 1s high-resolution scan of Fe<sub>3</sub>O<sub>4</sub>/HBPN can be deconvoluted into three individual peaks at binding energies of 398.6 eV, 399.1 eV and 400.2 eV (Figure 3b), which were assigned to the N atoms in the C–NH<sub>2</sub>, C–NH, and N–O groups [42–44], respectively. In the C 1s spectrum (Figure 3c), the C 1s peak in Fe<sub>3</sub>O<sub>4</sub>/HBPN was decomposed into three subpeaks at 284.9 eV, 285.6 eV and 287.9 eV, respectively. The peak at 284.9 eV belonged to the C–(C, H) from hydrocarbon-like compounds [45]. The second peak 285.6 was attributed to the –C or C–N or O–C–O bonds in amide polymers [46]. The third peak 287.6 eV corresponded to the C=O in groups from carboxylate [47]. As illustrated in Figure 3d, the peaks at 529.9 eV and 531.2 eV were, respectively, related to the chemical bonds between oxygen atoms and the Fe and –OH groups on the magnetic composite surface [48]. Also, the peaks related to 532.0 eV and 533.1 eV contributed to the lattice oxygen in Fe<sub>3</sub>O<sub>4</sub> and bidentate species (O–C=O), respectively [49,50].

As for Fe 2p peaks (Figure 3e), the two main peaks at 710.8 eV and 724.6 eV were attributed to Fe 2p<sub>3/2</sub> and Fe 2p<sub>1/2</sub> with peak areas of 59.6% and 40.4%, respectively. Also, the two peaks Fe 2p<sub>3/2</sub> and Fe 2p<sub>1/2</sub> were deconvoluted into Fe<sup>3+</sup> and Fe<sup>2+</sup>, and two doublets were split. Specifically, the peaks centered at 709.9 eV and 723.7 eV were, respectively, attributed to Fe<sup>2+</sup> 2p<sub>3/2</sub> (15.1%) and Fe<sup>2+</sup> 2p<sub>1/2</sub> (16.2%) split orbitals. Meanwhile, the deconvoluted peaks at 712.6 eV and 727.0 eV were attributed to Fe<sup>3+</sup> 2p<sub>3/2</sub> (30.4%) and Fe<sup>3+</sup> 2p<sub>1/2</sub> (38.7%) split orbitals, correspondingly [51–53]. The Fe<sup>2+</sup>/Fe<sup>3+</sup> ion ratio for Fe 2p<sub>3/2</sub> was found to be 0.49, which was close to 0.50, which was obtained from the atomic ratio contained in the naked Fe<sub>3</sub>O<sub>4</sub> particles. The above-mentioned results confirmed the presence of amine groups from HBPN in the synthesized Fe<sub>3</sub>O<sub>4</sub>/HBPN composites, and the coating mechanism of Fe<sub>3</sub>O<sub>4</sub>/HBPN composites was mainly due to the –C–NH<sub>2</sub> or –C–NH linkages of HBPN polymers, which bonded to the Fe<sub>3</sub>O<sub>4</sub> particles via the N–O bonds in the convolving process between loading sites of Fe<sub>3</sub>O<sub>4</sub> and HBPN polymers.

#### 2.1.4. SEM and EDS

The surface morphology of Fe<sub>3</sub>O<sub>4</sub> and Fe<sub>3</sub>O<sub>4</sub>/HBPN was determined by FE-SEM (Figure 4a–f). The Fe<sub>3</sub>O<sub>4</sub> particles presented an irregular granular morphology with different sizes, a block-like structure, a smooth surface and wrinkled edges. The irregular granular morphology may be owing to the co-precipitation method of Fe<sub>3</sub>O<sub>4</sub> preparation [54]. In contrast, the Fe<sub>3</sub>O<sub>4</sub>/HBPN composites clumped together and were loaded with an oil-like film after HBPN coating (Figure 4e,f). The high magnification image of Fe<sub>3</sub>O<sub>4</sub>/HBPN showed that the membranous-like structure was enveloped and wrapped around the Fe<sub>3</sub>O<sub>4</sub> particles. These membranous-like structures on the Fe<sub>3</sub>O<sub>4</sub>/HBPN surface may be formed due to the high viscosity and high polymerization characteristics [55,56].

The surface elements of Fe<sub>3</sub>O<sub>4</sub> and Fe<sub>3</sub>O<sub>4</sub>/HBPN are shown by the EDS spectrum analysis. As shown in Table 1, the main elements of the Fe<sub>3</sub>O<sub>4</sub> sample are Fe and O. The wt% ratio of Fe and O was 2.87, which proved the successfully prepared of Fe<sub>3</sub>O<sub>4</sub>. For the Fe<sub>3</sub>O<sub>4</sub>/HBPN, the main elements were C, N, O, Si and Fe. Relative to Fe<sub>3</sub>O<sub>4</sub>, the appearance of C and N elements illustrated that the results of elemental analysis were consistent with the composition characteristics of the material, which further verified the successful synthesis of the material.

**Table 1.** The EDS value of Fe<sub>3</sub>O<sub>4</sub> and Fe<sub>3</sub>O<sub>4</sub>/HBPN.

Fe <sub>3</sub> O <sub>4</sub>				Fe <sub>3</sub> O <sub>4</sub> /HBPN									
O		Fe		C		N		O		Si		Fe	
Wt%	At%	Wt%	At%	Wt%	At%	Wt%	At%	Wt%	At%	Wt%	At%	Wt%	At%
23.90	52.30	76.10	47.70	13.75	28.17	5.93	10.42	23.03	35.44	1.64	1.44	55.65	24.53
23.62	51.91	76.38	48.09	20.86	39.18	6.93	11.17	19.57	27.60	1.95	1.57	50.69	20.48
29.93	59.85	70.07	40.15	15.40	28.88	6.77	10.88	28.03	39.45	1.76	1.41	48.05	19.38

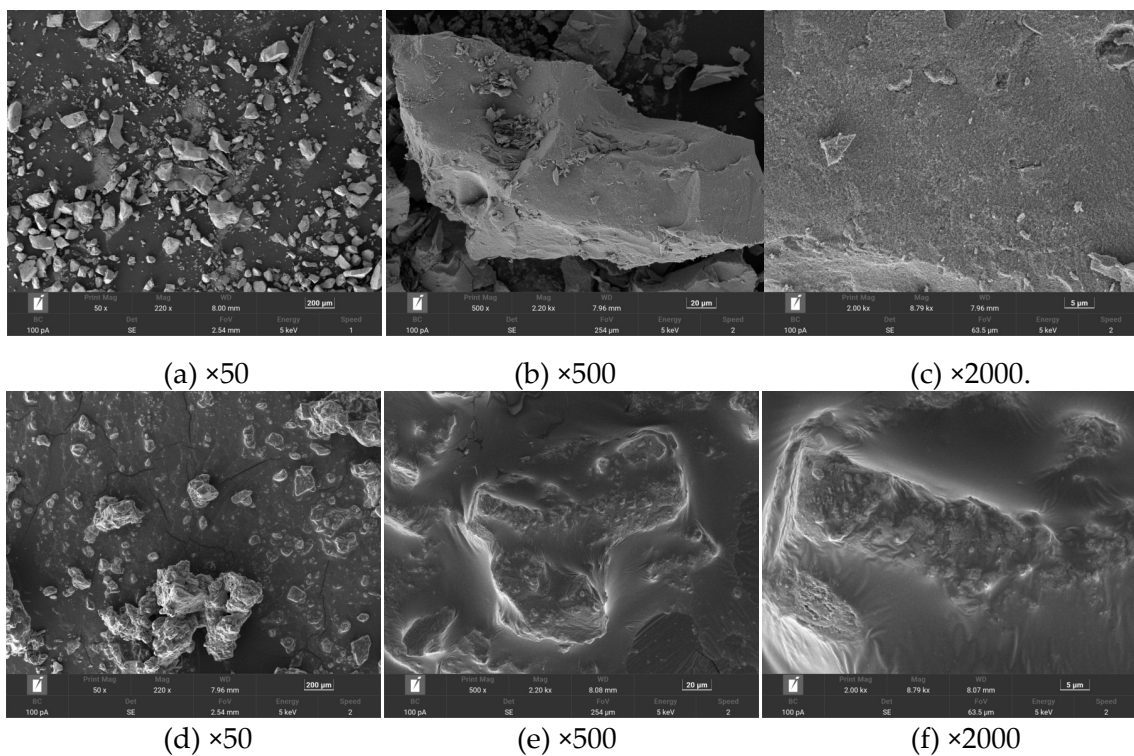


**Figure 4.** SEM images of  $\text{Fe}_3\text{O}_4$  (a–c) and  $\text{Fe}_3\text{O}_4/\text{HBPN}$  (d–f).

### 2.1.5. TGA

TGA is a process used to heat the analyzed samples and decompose them by breaking their chemical bonds, which is completed in order to assess the effect of thermal weightlessness and thermal stability [49,57,58]. Figure 5 shows the weight loss curves of  $\text{Fe}_3\text{O}_4$  and  $\text{Fe}_3\text{O}_4/\text{HBPN}$  against temperature changes, respectively. The weight loss of  $\text{Fe}_3\text{O}_4$  at 20–500 °C was about 6%, revealing a high content of  $\text{Fe}_3\text{O}_4$  with little impurity and humidity on its surface. In the temperature range of 500–800 °C, 0.9% mass loss appeared due to the thermal decomposition of the magnetite residue [59]. The results demonstrated that the  $\text{Fe}_3\text{O}_4$  particles exhibited excellent thermal stability.

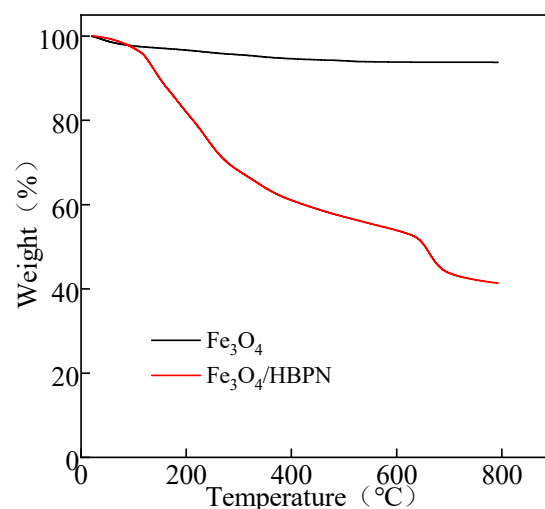


**Figure 5.** Thermogravimetric curves of  $\text{Fe}_3\text{O}_4$  and  $\text{Fe}_3\text{O}_4/\text{HBPN}$ .

The weight loss of  $\text{Fe}_3\text{O}_4/\text{HBPN}$  was analyzed through three stages at different temperature ranges. In the range of 20–110 °C, the weight loss was 3%, which was caused

by the thermal decomposition of residual organic solvents during the assembly process. There was a rapid weight loss (45%) in the range of 110–640 °C, which was due to the degradation of super-branched amino groups and alkyl [60]. Following, the weight loss was 10% from 500 to 800 °C, which was due to the chain-breaking thermal decomposition of HBPN, which was gradually carbonized. Overall, the mass loss curve of Fe<sub>3</sub>O<sub>4</sub>/HBPN exhibited an approximately linear trend, indicating that a constant weight loss occurred over the 20–800 °C ranges. Because the thermal stability of the composites mainly depends on the mass of the organic chemical groups, which was coated onto the surface of the target objects [61]; thus, the super-branched amino groups of –C–NH<sub>2</sub> and –C–NH will induce the degradation with increasing temperature.

#### 2.1.6. VSM

In order to study the magnetic properties of Fe<sub>3</sub>O<sub>4</sub> and Fe<sub>3</sub>O<sub>4</sub>/HBPN particles, the magnetic hysteresis loop was investigated; thus, the parameters of saturation magnetization (*M<sub>s</sub>*), remanent magnetization (*M<sub>r</sub>*), and coercive force (*H<sub>c</sub>*) could also be extracted. *M<sub>s</sub>* means the maximal magnetization value of magnetic particles, which magnetized as an external magnetic field was applied. Following, as the external magnetic field was removed, the magnetic particles still retained their remanent magnetization, which was named *M<sub>r</sub>*. In order to remove the remanent magnetization, an external field with an opposite direction of *M<sub>r</sub>* will be applied, and the strength of the opposite magnetic field is named *H<sub>c</sub>* [62–64]. Also, the value of *H<sub>c</sub>* exhibited the difficulty level of the magnetic particles to be magnetized.

In order to evaluate the magnetic properties, the Fe<sub>3</sub>O<sub>4</sub> and Fe<sub>3</sub>O<sub>4</sub>/HBPN samples were tested by VSM. As shown in Figure 6, the saturation magnetization (*M<sub>s</sub>*) value of the Fe<sub>3</sub>O<sub>4</sub> was 66.1 emu/g, while the *M<sub>s</sub>* value of Fe<sub>3</sub>O<sub>4</sub>/HBPN was attenuated to 33.7 emu/g. This was possibly because of the presence of amino-terminated hyperbranched polymers coated on Fe<sub>3</sub>O<sub>4</sub>, and the polymers were non-magnetic. However, the *M<sub>s</sub>* value of the Fe<sub>3</sub>O<sub>4</sub>/HBPN indicated that it was high enough to meet the requirement of magnetic separation by an external magnetic field. Moreover, the curves passed the origin of coordinates, which indicated that the coercivity (*H<sub>c</sub>*) and residual magnetization (*M<sub>r</sub>*) were close to zero, and there was almost no residual magnetic generation. It showed that Fe<sub>3</sub>O<sub>4</sub>/HBPN had superparamagnetic properties and a good magnetic response, so it was convenient for separation, recycle and reuse by recovering through an external magnetic field.

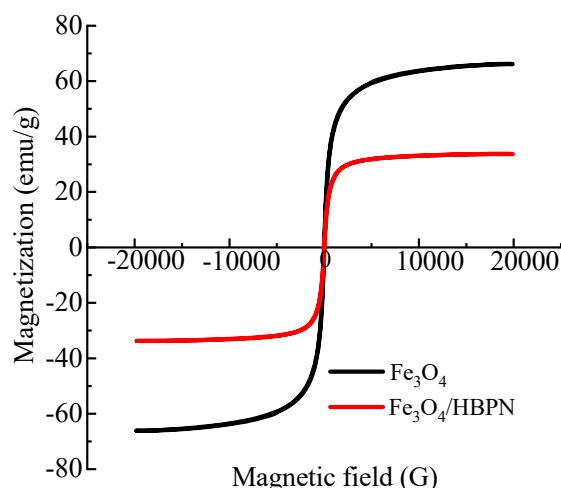


**Figure 6.** Magnetization hysteresis loops of Fe<sub>3</sub>O<sub>4</sub> and Fe<sub>3</sub>O<sub>4</sub>/HBPN.

#### 2.1.7. Zeta Potential

The zeta potential mainly investigates the occurrence of electric potential between the colloidal particles and bulk liquid, which causes the suspension of colloids [65]. As shown in Figure 7, the characteristic surface charge of Fe<sub>3</sub>O<sub>4</sub> and Fe<sub>3</sub>O<sub>4</sub>/HBPN was investigated by zeta potential measurement. The results showed that Fe<sub>3</sub>O<sub>4</sub> exhibited a negative charge

in the pH range 4–10. On the contrary,  $\text{Fe}_3\text{O}_4/\text{HBPN}$  showed a positive charge in the same pH range. This indicated that the zeta potential changed from negative to positive when the amino-terminated hyperbranched polymer assembled on  $\text{Fe}_3\text{O}_4$ . When the naked  $\text{Fe}_3\text{O}_4$  particles were dispersed in distilled water, the  $\text{Fe}_3\text{O}_4$  surface captured more  $\text{H}^+$  ions than  $\text{OH}^-$ . The hydrogen ions adsorbed on the  $\text{Fe}_3\text{O}_4$  surface, forming hydroxyl groups, which resulting in the naked  $\text{Fe}_3\text{O}_4$  being negatively charged [66–68]. In addition, the  $\text{H}^+$  from hydroxyl groups can react with amine groups such as  $-\text{NH}$ ,  $-\text{NH}_2$ ,  $-\text{N}^+$  and  $-\text{N}(\text{CH}_3)$  [69,70]. In the  $\text{Fe}_3\text{O}_4/\text{HBPN}$ , the dendritic structure with  $-\text{NH}_2$  displaced  $\text{H}^+$  ions on the  $\text{Fe}_3\text{O}_4$  surface, and the ionic exchange resulted in a positive charge on the  $\text{Fe}_3\text{O}_4$  surface, changing the zeta potential of  $\text{Fe}_3\text{O}_4/\text{HBPN}$  to positive. Thus, the zeta potential of  $\text{Fe}_3\text{O}_4/\text{HBPN}$  was positive.

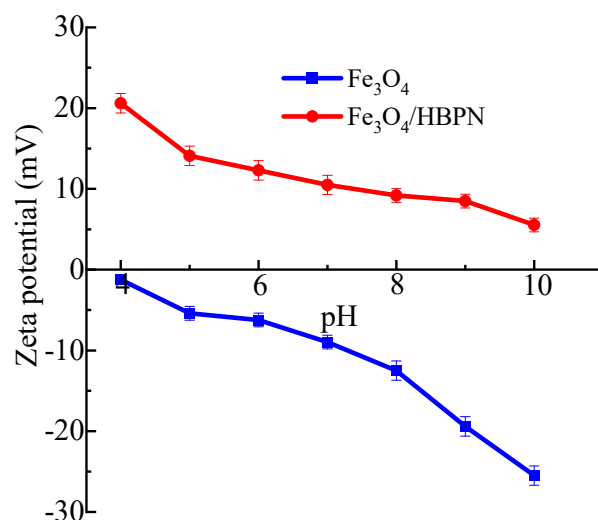


**Figure 7.** Zeta potential of  $\text{Fe}_3\text{O}_4$  and  $\text{Fe}_3\text{O}_4/\text{HBPN}$ .

## 2.2. Application Performance of $\text{Fe}_3\text{O}_4/\text{HBPN}$

### 2.2.1. Effects of Dosage

The kaolin-simulated high-turbidity wastewater was used to investigate the performance of  $\text{Fe}_3\text{O}_4/\text{HBPN}$ , and different influence factors including dosing concentration, pH, kaolin suspension concentration, magnetic field intensity were explored. As observed in Figure 8a, although the removal effect of all the dosages was increased before 5 min, there was already a noticeable difference. When the  $\text{Fe}_3\text{O}_4/\text{HBPN}$  concentration was 2.5 mg/L, the removal efficiency of kaolin was 80% in 5 min, and it reached 87% in 30 min (Figure 8b). In the first echelon, the removal effect was similar to 3.0 mg/L and 4.0 mg/L. However, with the increase in  $\text{Fe}_3\text{O}_4/\text{HBPN}$  concentration, the removal effect was worse, and the kaolin removal efficiency was 44% in 30 min.

According to the zeta potential, the surface of  $\text{Fe}_3\text{O}_4/\text{HBPN}$  was positively charged, which neutralized and reacted with the negative charges on the surface of kaolin. The large kaolin magnetic flocs were formed and then trapped smaller flocs through the sweeping effect. At last, all magnetic flocs moved and settled along the magnetic field. In addition, the amino groups of  $\text{Fe}_3\text{O}_4/\text{HBPN}$  provided a large amount of adsorption sites to enhance the removal effect by bridging action, simultaneously. Unfortunately, when the  $\text{Fe}_3\text{O}_4/\text{HBPN}$  concentration was too high, a large electrostatic repulsion among the initially flocs was formed, resulting in the instability of the flocs and difficulty of generating and aggregating [71].

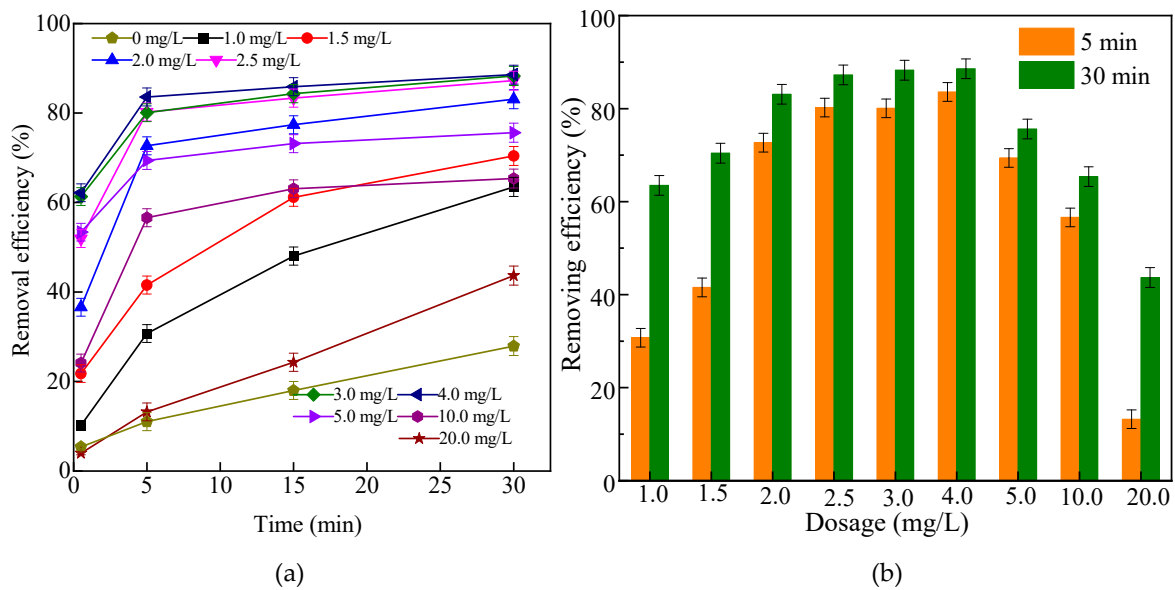


**Figure 8.** The effect of different dosages on kaolin suspension treatment at diverse times (a) and fixed times (b). (Ph = 5.6, kaolin suspension concentration was 1.0 g/L, magnetic field intensity was 3800 G).

### 2.2.2. Effects of pH

As shown in Figure 9, when the pH was 4–5,  $\text{Fe}_3\text{O}_4/\text{HBPN}$  showed a good removal performance of kaolin, and the removal effect was 88% in 30 min. On the contrary,  $\text{Fe}_3\text{O}_4/\text{HBPN}$  performed worse in alkaline conditions; the kaolin removal effect was less than 30% in 30 min. The results indicated that  $\text{Fe}_3\text{O}_4/\text{HBPN}$  had good flocculation characteristics in acidic environments. When the pH was 4–5, the zeta potential value of  $\text{Fe}_3\text{O}_4/\text{HBPN}$  was close to the negatively charged kaolin. At this time, the amino group ( $-\text{NH}_2$ ) was protonated into  $-\text{NH}_3^+$ , which made it easy to react with negatively charged kaolin, and it was integrated into larger magnetic flocs [72]. When the pH increased to alkaline,  $\text{Fe}_3\text{O}_4/\text{HBPN}$  still carried a positive charge, but the zeta potential value decreased significantly, and it was difficult for  $-\text{NH}_2$  to protonate. However, the zeta potential value of kaolin particles increased and carried a large amount of negative charge, which increased the electrostatic repulsion between particles and decreased the removal effect [73].

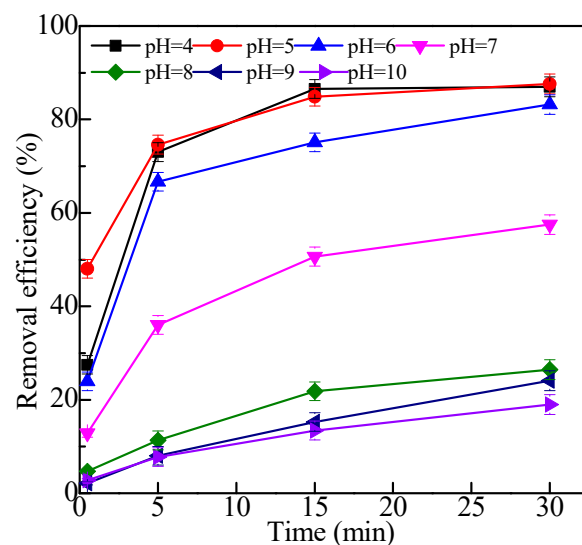


**Figure 9.** The effect of different pH on kaolin suspension treatment (the dosage was 2.5 mg/L, kaolin suspension concentration was 1.0 g/L, magnetic field intensity was 3800 G).

### 2.2.3. Effects of Concentration of Kaolin Suspensions

The removal effect of  $\text{Fe}_3\text{O}_4/\text{HBPN}$  at different kaolin concentrations is shown in Figure 10. When the kaolin concentration was 1.0 g/L, the removal performance of  $\text{Fe}_3\text{O}_4/\text{HBPN}$  was the best. The removal efficiency was 87% at 30 min, and it was significantly higher than other concentrations (0.5 g/L, 2.0 g/L, 5.0 g/L). This was because when the kaolin concentration was low, the  $\text{Fe}_3\text{O}_4/\text{HBPN}$  in solution was excessive, and the electrostatic repulsion among the flocs increased and inhibited the flocculation process. Moreover, the excessive kaolin concentration caused the amount of positive charge on the surface of  $\text{Fe}_3\text{O}_4/\text{HBPN}$  to be insufficient to neutralize the negative charge on the surface of kaolin particles.

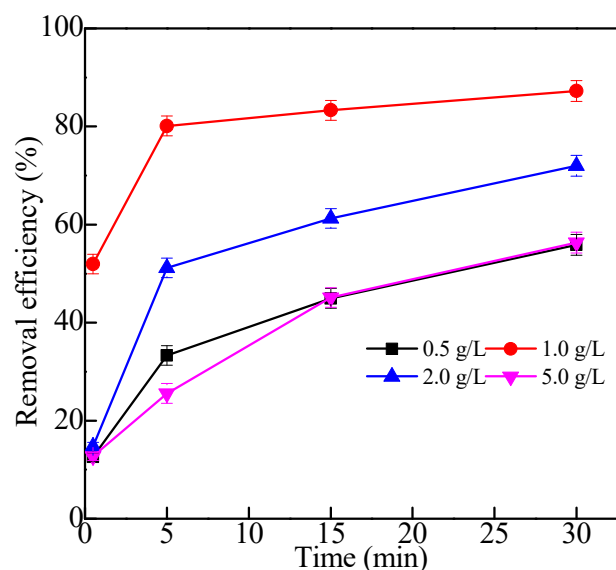


**Figure 10.** The treatment effect of different kaolin concentrations (the dosage was 2.5 mg/L, pH = 5.6, magnetic field intensity was 3800 G).

### 2.2.4. Effects of Magnetic Fields

Figure 11 showed the removal effect of magnetic field strength. It was obviously observed that the removal effect of  $\text{Fe}_3\text{O}_4/\text{HBPN}$  increased significantly with the increase in magnetic field intensity. When the magnetic field intensity increased from 500 to 3800 G, the removal efficiency of kaolin went up to 52% at 0.5 min, while it rose to 80% at 5 min. For the magnetic particles, the addition of the magnetic field contributed to the rapid moving of magnetic flocs, colliding with each other during the process of agglomeration [74]. It created more opportunities for the subsequent bridging and charge neutralization. In the process of magnetic flocs movement, the magnetic force received was positively correlated with the magnetic field intensity and gradient, and the magnetic field force played a very important role in magnetic flocculation separation. Therefore, with the increase in magnetic field intensity, the removal rate gradually increases [75].

In general, the optimum reaction conditions were obtained by conducting the series experiments. These showed that the dosage of  $\text{Fe}_3\text{O}_4/\text{HBPN}$  was 2.5 mg/L, pH = 5.6, magnetic field intensity was 3800 G, and the kaolin suspension concentration was 1.0 g/L. By comparing with some other reported material applied on kaolin removal (Table 2), it was found that although the removal effect of  $\text{Fe}_3\text{O}_4/\text{HBPN}$  was slightly inferior to others, the dosage of  $\text{Fe}_3\text{O}_4/\text{HBPN}$  was much lower than other materials. That means  $\text{Fe}_3\text{O}_4/\text{HBPN}$  was more economical in the application process.

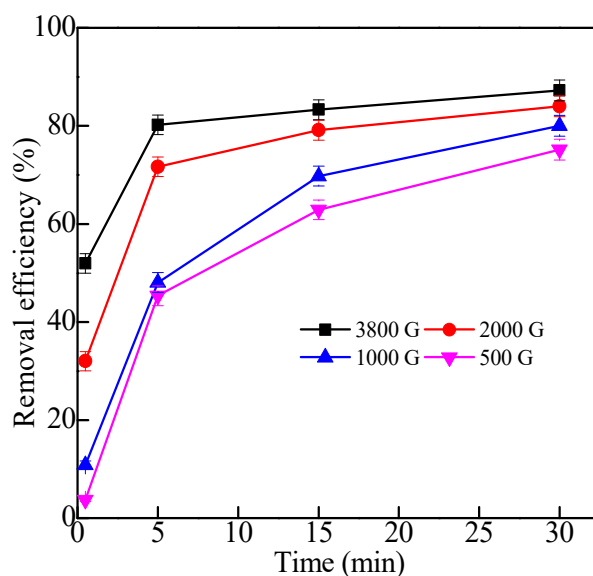


**Figure 11.** The effect of different magnetic fields intensity on kaolin suspension treatment (the dosage was 2.5 mg/L, pH = 5.6, kaolin suspension concentration was 1.0 g/L).

**Table 2.** The comparison of reported materials treated with kaolin.

Materials	Dosage	Treatment Capacity	Conference
Fe <sub>3</sub> O <sub>4</sub> /SiO <sub>2</sub>	1.0 g/L	93.8%	[15]
CE-PEI	0.15 mg/mL	98.2%	[71]
CPAMF	0.24 g/L	92.4%	[13]
FS@CTS-P	150 mg/L	92.54%	[76]
Fe <sub>3</sub> O <sub>4</sub> /HBPN	2.5 mg/L	87%	This paper

### 2.2.5. The Actual Water Application

The water samples from two lakes were treated with Fe<sub>3</sub>O<sub>4</sub>/HBPN, respectively, and the results are shown in Figure 12. The removal efficiency for Lake 1 was 86% at 30 min, while it was 87% for Lake 2. It indicated that Fe<sub>3</sub>O<sub>4</sub>/HBPN still showed a significant flocculation effect for actual water due to the charge neutralization and adsorption bridging effects. The generated floc could quickly separate under the action of applied magnetic fields and obtain a high-turbidity removal rate. Moreover, there was no obvious difference regarding the treatment effect between the simulated and actual water ( $p > 0.05$ ). When Fe<sub>3</sub>O<sub>4</sub>/HBPN was applied to actual water, the interference of complex water quality conditions was eliminated, and the flocculation effect was stable performance.

### 2.3. Recycling and Reusing

The recovery of Fe<sub>3</sub>O<sub>4</sub> particles from magnetic aggregates is an essential step, not only for particle recycle and reusing, but also for the downstream water treatment [77]. After Fe<sub>3</sub>O<sub>4</sub>/HBPN was used to treat kaolin suspensions, the material was separated from the solution via an external magnetic field. The recovered Fe<sub>3</sub>O<sub>4</sub>/HBPN was used again for the treatment of kaolin, and the operations were repeated five times to investigate the effect of regeneration and reusing. The recycling and reusing results are shown in Figure 13. Figure 13a shows the recycling efficiency of Fe<sub>3</sub>O<sub>4</sub> and Fe<sub>3</sub>O<sub>4</sub>/HBPN. The recycling efficiency of Fe<sub>3</sub>O<sub>4</sub> (92.3–94.5%) was slightly higher than that of Fe<sub>3</sub>O<sub>4</sub>/HBPN (91.2–93.2%), which is due to the fact that a small amount of functional groups loaded on the Fe<sub>3</sub>O<sub>4</sub>/HBPN surface fall off during separation. However, during the five recycling periods, there was no significant difference in RE regarding either Fe<sub>3</sub>O<sub>4</sub> or Fe<sub>3</sub>O<sub>4</sub>/HBPN ( $p > 0.05$ ). This showed that even if there was a small amount of loss in the application of Fe<sub>3</sub>O<sub>4</sub>/HBPN, the overall stability performed well.

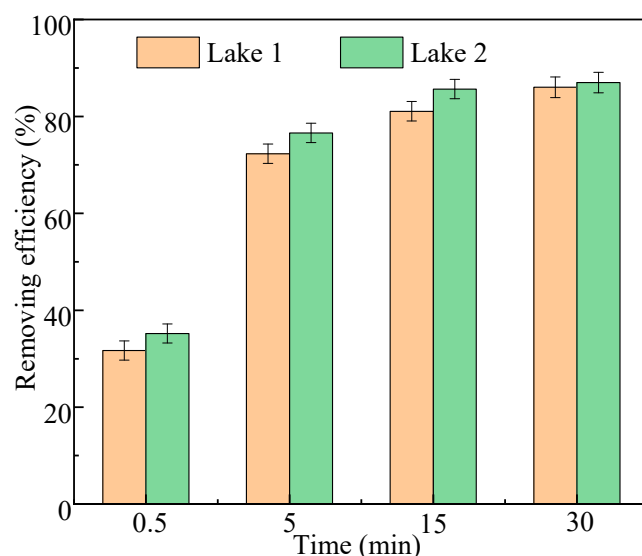


**Figure 12.** The actual water application effect in two lakes of Fe<sub>3</sub>O<sub>4</sub>/HBPN (the dosage was 2.5 mg/L, and the magnetic field intensity was 3800 G).

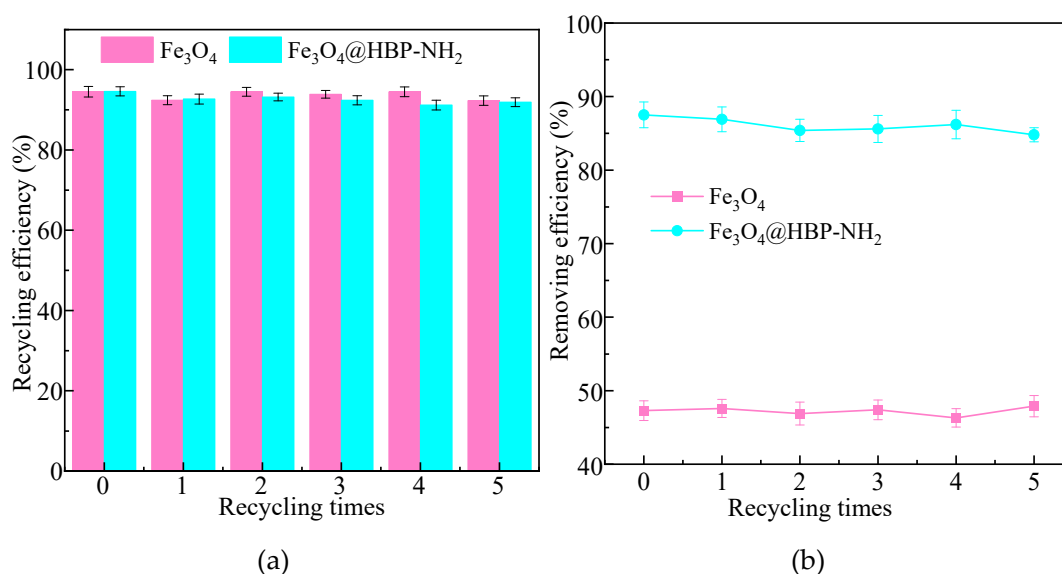


**Figure 13.** The recycling (a) and reusing (b) effect of Fe<sub>3</sub>O<sub>4</sub> and Fe<sub>3</sub>O<sub>4</sub>/HBPN (pH = 5.6, kaolin suspension concentration was 1.0 g/L, magnetic field intensity was 3800 G).

The reusing performance of Fe<sub>3</sub>O<sub>4</sub> and Fe<sub>3</sub>O<sub>4</sub>/HBPN is also shown in Figure 13b. As the control group, the removing efficiency of Fe<sub>3</sub>O<sub>4</sub> was from 46.3% to 47.9%, and it showed no significant difference five times ( $p > 0.05$ ). On the contrary, the removal efficiency of Fe<sub>3</sub>O<sub>4</sub>/HBPN before recycling was 87.5%, while the removal efficiency after 1–5 times recycling was in the range of 84.8%–86.9%. Although the removal efficiency before recycling was slightly higher than the subsequent recycled materials, there was no significant difference regarding the removal efficiency five times ( $p > 0.05$ ). At the beginning of the application, a small amount of functional groups fell from the material surface and resulted in the slight variation after reusing. However, the stability of Fe<sub>3</sub>O<sub>4</sub>/HBPN remained after several times recycling and reusing, and the removal efficiency stayed at a relatively stable level.

### 3. Materials and Methods

#### 3.1. Materials

Ferrous sulfate heptahydrate ( $\text{FeSO}_4 \cdot 7\text{H}_2\text{O}$ ), iron chloride hexahydrate ( $\text{FeCl}_3 \cdot 6\text{H}_2\text{O}$ ) and kaolin were purchased from Sinopharm Chemical Reagent Co., Ltd. (Shanghai, China). Ammonia ( $\text{NH}_3 \cdot \text{H}_2\text{O}$ ), methanol, ethanol, methyl acrylate and diethylenetriamine were obtained from Shanghai Macklin Biochemical Technology Co., Ltd. 3-aminopropyl trimethoxysilane (APTMs) was bought from Shanghai Aladdin Biochemical Technology Co., Ltd. All the chemical reagents were analytical grade and were used for without further pretreatment.

#### 3.2. Synthesis of magnetic $\text{Fe}_3\text{O}_4$ nanoparticles

The synthesis process of magnetic  $\text{Fe}_3\text{O}_4$  nanoparticles was used by the method of coprecipitation [78]. First, 2.7 g of  $\text{FeSO}_4 \cdot 7\text{H}_2\text{O}$  and 5.7 g of  $\text{FeCl}_3 \cdot 6\text{H}_2\text{O}$  (molar ratio: 2:1) were dissolved in 100 mL of deionized water. Then, the pH of the mixture solutions was adjusted to 10.0 by  $\text{NH}_3 \cdot \text{H}_2\text{O}$  solution, which was added dropwise and stirred vigorously on a magnetic stirrer at 25 °C. Once the mixture solution turned to black, the black precipitate was separated from the solution using a permanent magnet. Furthermore, the precipitate was heated to the temperature of 80 °C for 30 min and washed 3 times using alternate solutions of distilled water and ethanol. Then, the magnetic  $\text{Fe}_3\text{O}_4$  nanoparticles were obtained and free-dried.

#### 3.3. Preparation of Magnetic $\text{Fe}_3\text{O}_4$ /HBPN Composites

Firstly, the magnetic  $\text{Fe}_3\text{O}_4$  nanoparticles were dispersed in the solution of methanol (200 mL) using an ultrasonic bath for 30 min. Subsequently, 11.6 mL of APTMs was dropped to the stirring solution at 25 °C for 4 h, and the mixture was separated after intensive stirring, which involved washing with methanol. Next, 100 mL of methanol and 21.6 mL of methyl acrylate were added into the above mixture and stirred continuously for 7 h. Then, the magnetic mixture was separated and washed with methanol again. At last, 18.12 mL of diethylenetriamine and 25 mL of methanol were added into the magnetic mixture in a conical flask; afterwards, it was reacted in an oil bath at 65 °C for 1 h and 140 °C for 2 h, respectively, until the methanol evaporated. The final product in the flask consisted of hyperbranched magnetic composite  $\text{Fe}_3\text{O}_4$ /HBPN.

#### 3.4. Characterization of $\text{Fe}_3\text{O}_4$ /HBPN

The Fourier transform infrared (FTIR) spectra were monitored by employing a VERTEX 70 spectrometer (Bruker, Germany). The materials were grounded with KBr (1:100) and then compressed to form tables. The X-ray diffraction (XRD) patterns were collected with a Shimadzu XRD-7000 instrument at a scan rate of  $0.02^\circ \cdot \text{s}^{-1}$  with a  $2\theta$  range of  $20^\circ$ – $80^\circ$  and Cu  $K\alpha$  radiation ( $\lambda = 0.1542$  nm). XPS spectra were obtained via an Escalab 250 Xi spectrometer (Thermo Fisher Scientific Inc., Waltham, MA, USA) with a monochromated source of X-rays (Al  $K\alpha$ , 1486.6 photo energy) as the excitation source. SEM measurements were conducted on a TESCAN MIRA LMS microscope equipped with energy-dispersive X-ray spectrometry (Xplore 30, Oxford, UK). The thermal behavior analyses were conducted in an  $\text{N}_2$  atmosphere between room temperature and 800 °C at a rate of  $10^\circ \text{C} \cdot \text{min}^{-1}$  using a Q50 thermogravimetric analyzer (TA Instruments- Waters LLC, New Castle, DE, USA). The magnetic properties of the samples were measured using a LakeShore 7404S vibrational sample magnetometer (Lake Shore Cryotronics, Inc., Westerville, OH, USA). The thermal behavior analyses were conducted in an  $\text{N}_2$  atmosphere between room temperature and 800 °C at a rate of  $10^\circ \text{C} \cdot \text{min}^{-1}$  using a Q50 thermogravimetric analyzer (TA Instruments- Waters LLC, New Castle, DE, USA).

#### 3.5. The Magnetic Separation Experiment

In order to investigate the performance of  $\text{Fe}_3\text{O}_4$ /HBPN, the kaolin-simulated high-turbidity wastewater and natural water were employed in the research. The kaolin suspension was prepared using kaolin suspended in a 2.0 L volumetric flask with a concentration

of 2.0 g/L (1410 NTU). Except for the pH experiment, the pH of the kaolin suspensions was adjusted to 6.0.

The magnetic separation process was conducted in a jar test apparatus (ZR4-6, Zhongrun Water Industry Technology Development co., Ltd., China). The magnetic composite was first added to 400 mL kaolin suspensions (1.0 g/L) and then stirred for 1 min at 500 rpm; then, the beaker was placed inside a magnetic field created by a cubic NdFeB permanent magnet (50 mm L × 50 mm W × 25 mm H) with a magnetic induction intensity of 0.38 T. During magnetic separation, a 10 mL sample was collected from 3 cm below the solution surface at different time intervals (0.5, 5, 15, 30 min) to determine the concentration of kaolin. The separating efficiency (SE) was calculated using Equation (1):

$$\text{Separating efficiency(\%)} = \frac{x_0 - x_t}{x_0} \quad (1)$$

where  $x_0$  (mg/L) and  $x_t$  (mg/L) denote the initial kaolin concentration and kaolin concentration at time  $t$ , respectively.

The magnetic separation process was first tested at different dosages of magnetic composite Fe<sub>3</sub>O<sub>4</sub>/HBPN (1.0–20.0 mg/L). To investigate the effects of pH on separating, the pH of kaolin solution was adjusted in the range of 4–10, which using 1.0 mol/L HCl or 1.0 mol/L NaOH. Then, 0.5–5.0 g/L of kaolin concentrations was applied to explore the treatment effect. Different magnetic fields intensity of 500–3800 G were selected to test the kaolin removal effect. In the actual aqueous samples, the samples were taken freshly from two lakes in Luoyang City. To retain the accordant turbidity of the kaolin-simulated sample, moderate kaolin was added into the actual aqueous sample directly, keeping the turbidity at 1350–1450 NTU.

### 3.6. Recycle and Reuse of Fe<sub>3</sub>O<sub>4</sub>/HBPN

After the magnetic separation experiment, the supernatant was thoroughly removed from the beakers using a permanent magnet. The initial dosage of Fe<sub>3</sub>O<sub>4</sub>/HBPN was 2.5 mg/L. The magnetic aggregates were collected from all reaction vessels and dispersed in 5 mL of deionized water; then, the kaolin particles were detached from Fe<sub>3</sub>O<sub>4</sub>/HBPN composites by employing an ultrasonic generator (50 Hz, 1200 W) for 1 min. The recycled Fe<sub>3</sub>O<sub>4</sub>/HBPN composites were collected using the magnet (3800 G) and washed three times with deionized water. The recycled wet Fe<sub>3</sub>O<sub>4</sub>/HBPN composites were freeze-dried for further magnetic separation experiments. After weighing, Fe<sub>3</sub>O<sub>4</sub>/HBPN was evenly added to each reaction vessel to repeat the experiment. The recycling efficiency of Fe<sub>3</sub>O<sub>4</sub>/HBPN was calculated using Equation (2):

$$\text{recycling efficiency(\%)} = \frac{m_{i, \text{recovery}}}{m_{i, \text{dosing}}} \quad (2)$$

where  $m_{i, \text{recovery}}$  (mg) means the recovering weight of Fe<sub>3</sub>O<sub>4</sub>/HBPN, and  $m_{i, \text{dosing}}$  (mg) means the dosing weight of Fe<sub>3</sub>O<sub>4</sub>/HBPN at dosing time  $i$  ( $i = 0, 1, 2, \dots, 5$ ).

### 3.7. Analytical Methods

Zeta potentials were measured in a model environment (distilled water, pH 2–12) at 25 °C using a Zetasizer Nano (2000HSA, Malvern, UK). Measurements were taken for kaolin (1.0 g/L), Fe<sub>3</sub>O<sub>4</sub> (2.5 mg/L), Fe<sub>3</sub>O<sub>4</sub>/HBPN (2.5 mg/L) and recovered Fe<sub>3</sub>O<sub>4</sub>/HBPN. The supernatant after flocculation was detected directly. The pH of the solution was adjusted by 0.1 mol/L HCl and 0.1 mol/L NaOH, and the pH value was detected using a digital pH meter (PB-10, BSISL, China).

### 3.8. Statistical Analysis

The experiment data were analyzed using IBM SPSS 20 (SPSS Inc., Chicago, IL, USA). One-way analysis of variance (ANOVA) was employed to determine significant differences. A value of  $p < 0.05$  was considered to be significantly different.

## 4. Conclusions

A kind of magnetic composites ( $\text{Fe}_3\text{O}_4/\text{HBPN}$ ) was obtained by the embedded assembly of a three-dimensional amino-terminal hyperbranched polymer and  $\text{Fe}_3\text{O}_4$ . The  $-\text{C}-\text{NH}_2$  or  $-\text{C}-\text{NH}$  perssads of HBPN was linked with  $\text{Fe}_3\text{O}_4$  particles by N–O bonds, which changed the physicochemical characteristics of naked  $\text{Fe}_3\text{O}_4$ . The shape and size of  $\text{Fe}_3\text{O}_4/\text{HBPN}$  showed a different and uneven distribution; the particles clumped together and were coated with an oil-like film. Meanwhile,  $\text{Fe}_3\text{O}_4/\text{HBPN}$  showed a positive charge in the pH range 4–10 and exhibited superparamagnetic properties. In the treatment of high-turbidity wastewater,  $\text{Fe}_3\text{O}_4/\text{HBPN}$  performed best on the kaolin suspension under the conditions of adding a dosage of 2.5 mg/L, pH = 4–5, the kaolin concentration of 1.0 g/L, and the magnetic field of 3800 G. Whether using simulated wastewater or actual water, the removal efficiency reached 86%. The recycle efficiency of  $\text{Fe}_3\text{O}_4/\text{HBPN}$  was in the range of 91.2%–93.2%, while the removal efficiency of kaolin suspension achieved 84.8% after five recycling and reuse cycles. These results show that  $\text{Fe}_3\text{O}_4/\text{HBPN}$  has strong structural stability for the efficient treatment of high-turbidity wastewater.

**Author Contributions:** Conceptualization, Y.Z. and Q.F.; methodology, Q.F., Y.Z. and Y.L.; data analysis, X.W., S.W., X.G., M.Z. and L.G.; validation, Y.Z., Q.F.; writing—original draft preparation, Y.Z., Q.F., Y.L., M.Z. and X.W.; writing—review and editing, Y.Z., S.W., X.G. and L.G.; visualization and supervision, Y.Z., Q.F. and Y.L.; resources, Q.F. and Y.Z.; project administration and funding acquisition, Y.Z. and Q.F. All authors have read and agreed to the published version of the manuscript.

**Funding:** This work was financially supported in part by the Natural Science Foundation of Henan Province, China (No. 212300410138), the National Natural Science Foundation of China (42207493), the Guangdong Basic and Applied Basic Research Foundation (2020A1515110525), and the Student Research and Training Program of Henan University of Science and Technology (No. 2023182).

**Institutional Review Board Statement:** Not applicable.

**Informed Consent Statement:** Not applicable.

**Data Availability Statement:** The data presented in this study are available on request from the corresponding author.

**Acknowledgments:** The authors would like to thank Shiyanjia lab ([www.shiyanjia.com](http://www.shiyanjia.com), accessed on 16 August 2023) for XPS and VSM analysis.

**Conflicts of Interest:** The authors declare no conflict of interest.

**Sample Availability:** Not available.

## References

1. Xia, X.; Lan, S.; Li, X.; Xie, Y.; Liang, Y.; Yan, P.; Chen, Z.; Xing, Y. Characterization and coagulation-flocculation performance of a composite flocculant in high-turbidity drinking water treatment. *Chemosphere* **2018**, *206*, 701–708. [[CrossRef](#)] [[PubMed](#)]
2. Nie, Y.; Wang, Z.; Zhang, R.; Ma, J.; Zhang, H.; Li, S.; Li, J. *Aspergillus oryzae*, a novel eco-friendly fungal bioflocculant for turbid drinking water treatment. *Sep. Purif. Technol.* **2021**, *279*, 119669. [[CrossRef](#)]
3. Shabanizadeh, H.; Taghavijelouidar, M. A sustainable approach for industrial wastewater treatment using *pomegranate* seeds in flocculation-coagulation process: Optimization of COD and turbidity removal by response surface methodology (RSM). *J. Water Process Eng.* **2023**, *53*, 103651. [[CrossRef](#)]
4. Liu, X.; Xia, J.; Zu, J.; Zeng, Z.; Li, Y.; Li, J.; Wang, Q.; Liu, Z.; Cai, W. Spatiotemporal variations and gradient functions of water turbidity in shallow lakes. *Ecol. Indic.* **2023**, *147*, 109928. [[CrossRef](#)]
5. Song, S.; Le-Clech, P.; Shen, Y. Microscale fluid and particle dynamics in filtration processes in water treatment: A review. *Water Res.* **2023**, *233*, 119746. [[CrossRef](#)]
6. Zhao, K.; Wei, Y.; Dong, J.; Zhao, P.; Wang, Y.; Pan, X.; Wang, J. Separation and characterization of microplastic and nanoplastic particles in marine environment. *Environ. Pollut.* **2022**, *297*, 118773. [[CrossRef](#)]

7. Bokhari, T.H.; Sultana, H.; Usman, M. Adsorptive micellar flocculation (surfactant-based phase separation technique): Theory and applications. *J. Mol. Liq.* **2020**, *323*, 115001.
8. Xu, S.; Shi, J.; Deng, J.; Sun, H.; Wu, J.; Ye, Z. Flocculation and dewatering of the Kaolin slurry treated by single- and dual-polymer flocculants. *Chemosphere* **2023**, *328*, 138445. [[CrossRef](#)]
9. Cruz, D.; Pimentel, M.; Russo, A.; Cabral, W. Charge neutralization mechanism efficiency in water with high color turbidity ratio using aluminium sulfate and flocculation index. *Water* **2020**, *12*, 572. [[CrossRef](#)]
10. Zhou, L.; Han, Y.; Li, W.; Zhu, Y. Study on polymer-bridging flocculation performance of ultrafine specular hematite ore and its high gradient magnetic separation behavior: Description of floc microstructure and flocculation mechanism. *Sep. Purif. Technol.* **2021**, *276*, 119304. [[CrossRef](#)]
11. Housni, S.; Abramson, S.; Guigner, J.M.; Levitz, P.; Michot, L. Flocculation and magnetically-assisted sedimentation of size-sorted beidellite platelets mixed with maghemite nanoparticles. *Nano Res.* **2020**, *13*, 3001–3011. [[CrossRef](#)]
12. Lee, H.K.; Kim, J.H.; Kim, I.; Jeon, H. Efficient separation performance of suspended soil and strontium from aqueous solution using magnetic flocculant. *J. Environ. Chem. Eng.* **2021**, *9*, 106810. [[CrossRef](#)]
13. Ma, J.; Fu, X.; Jiang, L.; Zhu, G.; Shi, J. Magnetic flocculants synthesized by Fe<sub>3</sub>O<sub>4</sub> coated with cationic polyacrylamide for high turbid water flocculation. *Environ. Sci. Pollut. Res.* **2018**, *25*, 25955–25966. [[CrossRef](#)]
14. Zhao, Y.; Liu, Y.; Xu, H.; Fan, Q.; Zhu, C.; Liu, J.; Zhu, M.; Wang, X.; Niu, A. Preparation and application of magnetic composites using controllable assembly for use in water treatment: A review. *Molecules* **2023**, *28*, 5799. [[CrossRef](#)] [[PubMed](#)]
15. Liu, C.; Wang, X.; Qin, L.; Li, H.; Liang, W. Magnetic coagulation and flocculation of a kaolin suspension using Fe<sub>3</sub>O<sub>4</sub> coated with SiO<sub>2</sub>. *J. Environ. Chem. Eng.* **2021**, *9*, 105980. [[CrossRef](#)]
16. Wang, T.; Yang, W.; Hong, Y.; Hou, Y. Magnetic nanoparticles grafted with amino-riched dendrimer as magnetic flocculant for efficient harvesting of oleaginous microalgae. *Chem. Eng. J.* **2016**, *297*, 304–314. [[CrossRef](#)]
17. Perez, T.; Pasquini, D.; Lima, A.d.F.; Rosa, E.V.; Sousa, M.H.; Cerqueira, D.A.; de Moraes, L.C. Efficient removal of lead ions from water by magnetic nanosorbents based on manganese ferrite nanoparticles capped with thin layers of modified biopolymers. *J. Environ. Chem. Eng.* **2019**, *7*, 102892. [[CrossRef](#)]
18. Zhao, Y.; Liang, W.; Liu, L.; Li, F.; Fan, Q.; Sun, X. Harvesting *Chlorella vulgaris* by magnetic flocculation using Fe<sub>3</sub>O<sub>4</sub> coating with polyaluminium chloride and polyacrylamide. *Bioresour. Technol.* **2015**, *198*, 789–796. [[CrossRef](#)]
19. Zhang, J.; Tian, X.; Cui, X.; Zheng, A.; Li, J.; Bai, Y.; Zheng, Y. Facile synthesis of hyperbranched magnetic nanomaterials for selective adsorption of proteins. *Talanta* **2023**, *252*, 123895. [[CrossRef](#)]
20. Liu, Z.; Xu, Q.; Yan, C.; Li, J.; Zhou, W.; Gao, H.; Zhang, S.; Lu, R. Hyperbranched aromatic polyamide modified magnetic nanoparticles for the extraction of benzoylurea insecticides. *J. Sep. Sci.* **2021**, *44*, 1931–1938. [[CrossRef](#)]
21. Huo, L.; Zhang, Z.; Shi, X. Latest research and developing tendency of hyperbranched polymers fabrication. *J. Polym. Res.* **2021**, *28*, 355. [[CrossRef](#)]
22. Chen, S.; Xu, Z.; Zhang, D. Synthesis and application of epoxy-ended hyperbranched polymers. *Chem. Eng. J.* **2018**, *343*, 283–302. [[CrossRef](#)]
23. Ahmadi, Y.; Kim, K.H. Hyperbranched polymers as superior adsorbent for the treatment of dyes in water. *Adv. Colloid Interface Sci.* **2022**, *302*, 102633. [[CrossRef](#)] [[PubMed](#)]
24. Ghazi, M.L.; Ganjaee, S.M.; Bahram, R. Polyester-amide hyperbranched polymer as an interfacial modifier for graphene oxide nanosheets: Mechanistic approach in an epoxy nanocomposite coating. *Prog. Org. Coat.* **2020**, *142*, 105573. [[CrossRef](#)]
25. Wan, W.; Hui, O.; Jiang, Z.; Cui, Y.; Li, J.; He, M.; Yang, S.; Zhang, X.; Feng, Y.; Wei, Y. Synthesis and intracellular drug delivery applications of hyperbranched polymers functionalized β-cyclodextrin. *Colloid Interface Sci. Commun.* **2021**, *42*, 100425. [[CrossRef](#)]
26. Liu, Z.; Lin, X.; Liu, X.; Li, J.; Zhou, W.; Gao, H.; Zhang, S.; Lu, R. Magnetic nanoparticles modified with hyperbranched polyamidoamine for the extraction of benzoylurea insecticides prior to their quantitation by HPLC. *Microchim. Acta* **2019**, *186*, 351. [[CrossRef](#)] [[PubMed](#)]
27. Li, Z.; Wu, J.; Chen, P.; Zeng, Q.; Wen, X.; Wen, W.; Liu, Y.; Chen, A.; Guan, J.; Liu, X.; et al. A new metallic composite cathode originated from hyperbranched polymer coated MOF for High-performance Lithium-Sulfur batteries. *Chem. Eng. J.* **2022**, *435*, 135125. [[CrossRef](#)]
28. Malekzadeh, A.M.; Ramazani, A.; Rezaei, S.J.T.; Niknejad, H. Design and construction of multifunctional hyperbranched polymers coated magnetite nanoparticles for both targeting magnetic resonance imaging and cancer therapy. *J. Colloid Interface Sci.* **2017**, *490*, 64–73. [[CrossRef](#)]
29. Tian, W.; Li, X.; Wang, J. Supramolecular hyperbranched polymers. *Chem. Commun.* **2017**, *53*, 2531–2542. [[CrossRef](#)]
30. Belgaoankar, M.S.; Balasubramanian, K. Hyperbranched polymer-based nanocomposites: Synthesis, progress, and applications. *Eur. Polym. J.* **2021**, *147*, 110301. [[CrossRef](#)]
31. Hasan, K.; Joseph, R.G.; Patole, S.P.; Al-Qawasmeh, R.A. Development of magnetic Fe<sub>3</sub>O<sub>4</sub>-chitosan immobilized Cu(II) Schiff base catalyst: An efficient and reusable catalyst for microwave assisted one-pot synthesis of propargylamines via A<sup>3</sup> coupling. *Catal. Commun.* **2023**, *174*, 106588. [[CrossRef](#)]
32. Yeamsuksawat, T.; Zhao, H.; Liang, J. Characterization and antimicrobial performance of magnetic Fe<sub>3</sub>O<sub>4</sub>@Chitosan@Ag nanoparticles synthesized via suspension technique. *Mater. Today Commun.* **2021**, *28*, 102481. [[CrossRef](#)]
33. Calahorra-Rio, L.; Guadano-Sanchez, M.; Moya-Cavas, T.; Urraca, J.L. Magnetic core-shell nanoparticles using molecularly imprinted polymers for zearalenone determination. *Molecules* **2022**, *27*, 8166. [[CrossRef](#)] [[PubMed](#)]

34. Bilkan, M.T.; Yurdakul, Ş.; Demircioğlu, Z.; Büyükgüngör, O. Crystal structure, FT-IR, FT-Raman and DFT studies on a novel compound  $[C_{10}H_9N_3]_4AgNO_3$ . *J. Organomet. Chem.* **2016**, *805*, 108–116. [[CrossRef](#)]
35. Zhao, Y.; Wang, X.; Jiang, X.; Fan, Q.; Li, X.; Jiao, L.; Liang, W. Harvesting of *Chlorella vulgaris* using  $Fe_3O_4$  coated with modified plant polyphenol. *Environ. Sci. Pollut. Res.* **2018**, *25*, 26246–26258. [[CrossRef](#)]
36. Balkanloo, P.G.; Mahmoudian, M.; Hosseinzadeh, M.T. A comparative study between MMT- $Fe_3O_4$ /PES, MMT-HBE/PES, and MMT-acid activated/PES mixed matrix membranes. *Chem. Eng. J.* **2020**, *396*, 125188. [[CrossRef](#)]
37. Tariq, A.; Aamir, M.; Farhat Mehmood, R.; Akhtar, J.; Sher, M. Nanostructured  $Fe_3O_4@SiO_2$  shell-coated APTES/AEAPS as an efficient and recyclable catalyst for selective N-alkylation of amines using alcohol. *Mater. Today: Proc.* **2022**, *53*, 361–368. [[CrossRef](#)]
38. Seal, P.; Alam, A.; Borgohain, C.; Paul, N.; Babu, P.D.; Borah, J.P. Optimization of self heating properties of  $Fe_3O_4$  using PEG and amine functionalized MWCNT. *J. Alloys Compd.* **2021**, *882*, 160653. [[CrossRef](#)]
39. Wu, G.; Tu, H.; Niu, F.; Lu, S.; Liu, Y.; Gao, K.; Chen, Z.; Wang, P.; Li, Z. Synthesis of polymer-functionalized  $\beta$ -cyclodextrin,  $Mg^{2+}$  doped, coating magnetic  $Fe_3O_4$  nanoparticle carriers for penicillin G acylase immobilization. *Colloids Surf. A Physicochem. Eng. Asp.* **2023**, *657*, 130609. [[CrossRef](#)]
40. Lu, M.; Liu, M.; Wang, L.; Xu, S.; Zhao, J.; Li, H. Structural and magnetic properties of  $CoFe_2O_4/CoFe_2/SiO_2$  nanocomposites with exchange coupling behavior. *J. Alloys Compd.* **2017**, *690*, 27–30. [[CrossRef](#)]
41. Zhang, Y.; Zhu, T.; Xu, Y.; Yang, Y.; Sheng, D.; Ma, Q. Quaternized salicylaldehyde Schiff base side-chain polymer-grafted magnetic  $Fe_3O_4$  nanoparticles for the removal and detection of  $Cu^{2+}$  ions in water. *Appl. Surf. Sci.* **2023**, *611*, 155632. [[CrossRef](#)]
42. Shen, H.; Chen, Z.; Li, Z.; Hu, M.; Dong, X.; Xia, Q. Controlled synthesis of 2,4,6-trichlorophenol-imprinted amino-functionalized nano- $Fe_3O_4$ -polymer magnetic composite for highly selective adsorption. *Colloids Surf. A Physicochem. Eng. Asp.* **2015**, *481*, 439–450. [[CrossRef](#)]
43. Deng, Z.; Luo, Y.; Bian, M.; Guo, X.; Zhang, N. Synthesis of easily renewable and recoverable magnetic PEI-modified  $Fe_3O_4$  nanoparticles and its application for adsorption and enrichment of tungsten from aqueous solutions. *Environ. Pollut.* **2023**, *330*, 121703. [[CrossRef](#)]
44. Sharifi, M.J.; Nouralishahi, A.; Hallajisani, A.  $Fe_3O_4$ -chitosan nanocomposite as a magnetic biosorbent for removal of nickel and cobalt heavy metals from polluted water. *Int. J. Biol. Macromol.* **2023**, *248*, 125984. [[CrossRef](#)]
45. Nagappan, S.; Duraivel, M.; Muthuchamy, N.; Han, S.H.; Mohan, B.; Park, S.; Prabakar, K.; Lee, J.M.; Park, K.H. Straightforward engineering of porous  $C_3N_4/Fe_3O_4$  electrocatalyst for oxygen reduction reaction in alkaline medium. *Mater. Today Chem.* **2023**, *30*, 101534. [[CrossRef](#)]
46. Ghobeira, R.; Tabaei, P.S.E.; Morent, R.; Geyter, N.D. Chemical characterization of plasma-activated polymeric surfaces via XPS analyses: A review. *Surf. Interfaces* **2022**, *31*, 102087. [[CrossRef](#)]
47. Ma, B.; Li, S.; Wang, S.; Gao, M.; Guo, L.; She, Z.; Zhao, Y.; Jin, C.; Yu, N.; Zhao, C. Effect of  $Fe_3O_4$  nanoparticles on composition and spectroscopic characteristics of extracellular polymeric substances from activated sludge. *Process Biochem.* **2018**, *75*, 212–220. [[CrossRef](#)]
48. Maslakov, K.I.; Teterin, Y.A.; Popel, A.J.; Teterin, A.Y.; Ivanov, K.E.; Kalmykov, S.N.; Petrov, V.G.; Springell, R.; Scott, T.B.; Farnan, I. XPS study of the surface chemistry of  $UO_2$  (111) single crystal film. *Appl. Surf. Sci.* **2017**, *433*, 582–588. [[CrossRef](#)]
49. Sitthichai, S.; Pilapong, C.; Thongtem, T.; Thongtem, S. CMC-coated  $Fe_3O_4$  nanoparticles as new MRI probes for hepatocellular carcinoma. *Appl. Surf. Sci.* **2015**, *356*, 972–977. [[CrossRef](#)]
50. Lu, J.; Fu, F.; Ding, Z.; Na, L.; Bing, T. Removal mechanism of selenite by  $Fe_3O_4$ -precipitated mesoporous magnetic carbon microspheres. *J. Hazard. Mater.* **2017**, *330*, 93–104. [[CrossRef](#)] [[PubMed](#)]
51. Hur, J.U.; Shin, J.R.; Han, J.S.; Kim, Y.H.; An, G.S. Self-assembled core-shell  $Fe_3O_4$ -Pt nanoparticles via silylation/polymerization-based amino-functionalization. *Colloid Interface Sci. Commun.* **2022**, *50*, 100655. [[CrossRef](#)]
52. El-Aal, M.A.; Said, A.E.-A.A.; Goda, M.N.; Abo Zeid, E.F.; Ibrahim, S.M.  $Fe_3O_4@CMC$ -Cu magnetic nanocomposite as an efficient catalyst for reduction of toxic pollutants in water. *J. Mol. Liq.* **2023**, *385*, 122317. [[CrossRef](#)]
53. Qi, J.; Zhang, J.; Jia, H.; Guo, X.; Yue, Y.; Yuan, Y.; Yue, T. Synthesis of silver/ $Fe_3O_4@chitosan@polyvinyl$  alcohol magnetic nanoparticles as an antibacterial agent for accelerating wound healing. *Int. J. Biol. Macromol.* **2022**, *221*, 1404–1414. [[CrossRef](#)]
54. Liu, C.; Jiang, X.; Wang, X.; Wang, Q.; Liang, W. Magnetic polyphenol nanocomposite of  $Fe_3O_4/SiO_2/PP$  for Cd(II) adsorption from aqueous solution. *Environ. Technol.* **2020**, *43*, 935–948. [[CrossRef](#)] [[PubMed](#)]
55. Zhan, F.; Xiong, L.; Liu, F.; Li, C. Grafting hyperbranched polymers onto  $TiO_2$  nanoparticles via thiol-yne click chemistry and its effect on the mechanical, thermal and surface properties of polyurethane coating. *Materials* **2019**, *12*, 2817. [[CrossRef](#)] [[PubMed](#)]
56. Kalbasi, R.J.; Zamani, F. Synthesis and characterization of Ni nanoparticles incorporated into hyperbranched polyamidoamine-polyvinylamine/SBA-15 catalyst for simple reduction of nitro aromatic compounds. *RSC Adv.* **2014**, *4*, 7444–7453. [[CrossRef](#)]
57. Oliva, F.S.N.; Sahihi, M.; Lenglet, L.; Ospina, A.; Guenin, E.; Jaramillo-Botero, A.; Goddard, W.A.; Bedoui, F. Nanoparticle size and surface chemistry effects on mechanical and physical properties of nano-reinforced polymers: The case of PVDF- $Fe_3O_4$  nano-composites. *Polym. Test.* **2023**, *117*, 107851. [[CrossRef](#)]
58. Vattathurvalappil, S.H.; Kundurthi, S.; Drzal, L.T.; Haq, M. Thermo-mechanical degradation in ABS- $Fe_3O_4$  polymer nanocomposite due to repeated electromagnetic heating. *Compos. Part B Eng.* **2020**, *201*, 108374. [[CrossRef](#)]

59. Bahadur, A.; Saeed, A.; Shoaib, M.; Iqbal, S.; Bashir, M.I.; Waqas, M.; Hussain, M.N.; Abbas, N. Eco-friendly synthesis of magnetite ( $\text{Fe}_3\text{O}_4$ ) nanoparticles with tunable size: Dielectric, magnetic, thermal and optical studies. *Mater. Chem. Phys.* **2017**, *198*, 229–235. [[CrossRef](#)]
60. Xia, Z.; Singh, A.; Kiratitanavit, W.; Mosurkal, R.; Kumar, J.; Nagarajan, R. Unraveling the mechanism of thermal and thermo-oxidative degradation of tannic acid. *Thermochim. Acta* **2015**, *605*, 77–85. [[CrossRef](#)]
61. Thébault, M.; Pizzi, A.; Essawy, H.A.; Barhoum, A.; Assche, G.V. Isocyanate free condensed tannin-based polyurethanes. *Eur. Polym. J.* **2015**, *67*, 513–526. [[CrossRef](#)]
62. Venkateswarlu, S.; Kumar, S.H.; Jyothi, N.V.V. Rapid removal of Ni(II) from aqueous solution using 3-Mercaptopropionic acid functionalized bio magnetite nanoparticles. *Water Resour. Ind.* **2015**, *12*, 1–7. [[CrossRef](#)]
63. Cui, K.; Yuan, L.; Zhao, Z. Magnetic properties of  $\text{Ni}_3\text{Si}/\text{Fe}_3\text{O}_4$ @PVDF composites with different  $\text{Fe}_3\text{O}_4$  nanoparticles content based on lamellar  $\text{Ni}_3\text{Si}$  template. *Mater. Sci. Eng. B* **2023**, *290*, 116330. [[CrossRef](#)]
64. Mou, F.Z.; Guan, J.G.; Ma, H.R.; Xu, L.L.; Shi, W.D. Magnetic iron oxide chestnutlike hierarchical nanostructures: Preparation and their excellent arsenic removal capabilities. *ACS Appl. Mater. Interfaces* **2012**, *4*, 3987–3993. [[CrossRef](#)] [[PubMed](#)]
65. Hamid, S.H.A.; Lananan, F.; Wan, N.S.D.; Su, S.L.; Khatoun, H.; Endut, A.; Jusoh, A. Harvesting microalgae, *Chlorella sp.* by bio-flocculation of *Moringa oleifera* seed derivatives from aquaculture wastewater phytoremediation. *Int. Biodeterior. Biodegrad.* **2014**, *95*, 270–275. [[CrossRef](#)]
66. Liu, P.; Wang, T.; Yang, Z.; Hong, Y.; Hou, Y. Long-chain poly-arginine functionalized porous  $\text{Fe}_3\text{O}_4$  microspheres as magnetic flocculant for efficient harvesting of oleaginous microalgae. *Algal Res.* **2017**, *27*, 99–108. [[CrossRef](#)]
67. Zhao, Y.; Fan, Q.; Wang, X.; Jiang, X.; Jiao, L.; Liang, W. Application of  $\text{Fe}_3\text{O}_4$  coated with modified plant polyphenol to harvest oleaginous microalgae. *Algal Res.* **2019**, *38*, 101417. [[CrossRef](#)]
68. Ma, M.; Zhang, Y.; Yu, W.; Shen, H.Y.; Zhang, H.Q.; Gu, N. Preparation and characterization of magnetite nanoparticles coated by amino silane. *Colloids Surf. A Physicochem. Eng. Asp.* **2003**, *212*, 219–226. [[CrossRef](#)]
69. Toh, P.Y.; Ng, B.W.; Chong, C.; Ahmad, A.L.; Yang, J.W.; Derek, C.J.C.; Lim, J.K. Magnetophoretic separation of microalgae: The role of nanoparticles and polymer binder in harvesting biofuel. *RSC Adv.* **2014**, *4*, 4114–4121. [[CrossRef](#)]
70. Wang, S.; Stiles, A.R.; Guo, C.; Liu, C. Harvesting microalgae by magnetic separation: A review. *Algal Res.* **2015**, *9*, 178–185. [[CrossRef](#)]
71. Li, Z.; Gong, W.; Chen, X.; Liu, L.; Meng, R.; Ding, Y.; Yao, J. Sustainable cationic cellulose for highly efficient flocculation of Kaolin suspension. *Cellulose* **2021**, *28*, 11097–11108. [[CrossRef](#)]
72. Liu, B.; Zheng, H.; Wang, Y.; Chen, X.; Zhao, C.; An, Y.; Tang, X. A novel carboxyl-rich chitosan-based polymer and its application for clay flocculation and cationic dye removal. *Sci. Total Environ.* **2018**, *640–641*, 107–115. [[CrossRef](#)] [[PubMed](#)]
73. Li, Z.; Gui, X.; Cao, Y.; Gao, L.; Li, S. Effect of pH on the flocculation behaviors of kaolin using a pH-sensitive copolymer. *Water Sci. Technol.* **2016**, *74*, 729–737. [[CrossRef](#)] [[PubMed](#)]
74. Xiao, X.; Yu, Y.; Sun, Y.; Zheng, X.; Chen, A. Heavy metal removal from aqueous solutions by chitosan-based magnetic composite flocculants. *J. Environ. Sci.* **2021**, *108*, 22–32. [[CrossRef](#)] [[PubMed](#)]
75. Yu, W.; Wang, C.; Wang, G.; Feng, Q. Flocculation performance and kinetics of magnetic polyacrylamide microsphere under different magnetic field strengths. *J. Chem.* **2020**, *2020*, 1579424. [[CrossRef](#)]
76. Liu, C.; Wang, X.; Du, S.; Liang, W. Synthesis of chitosan-based grafting magnetic flocculants for flocculation of kaolin suspensions. *J. Environ. Sci.* **2024**, *139*, 193–205. [[CrossRef](#)]
77. Seo, J.Y.; Praveenkumar, R.; Kim, B.; Seo, J.C.; Park, J.Y.; Na, J.G.; Sang, G.J.; Park, S.B.; Lee, K.; Oh, Y.K. Downstream integration of microalgae harvesting and cell disruption by means of cationic surfactant-decorated  $\text{Fe}_3\text{O}_4$  nanoparticles. *Green Chem.* **2016**, *18*, 3981–3989. [[CrossRef](#)]
78. Antarnusa, G.; Jayanti, P.D.; Denny, Y.R.; Suherman, A. Utilization of co-precipitation method on synthesis of  $\text{Fe}_3\text{O}_4$  PEG. *Materialia* **2022**, *25*, 101525. [[CrossRef](#)]

**Disclaimer/Publisher’s Note:** The statements, opinions and data contained in all publications are solely those of the individual author(s) and contributor(s) and not of MDPI and/or the editor(s). MDPI and/or the editor(s) disclaim responsibility for any injury to people or property resulting from any ideas, methods, instructions or products referred to in the content.